Energy & Environmental Science

ROYAL SOCIETY OF CHEMISTRY

PAPER

View Article Online
View Journal | View Issue

Cite this: *Energy Environ. Sci.*, 2025, **18**, 9917

Balancing the supersaturation rate and coordination capability for upscaling high-performance perovskite photovoltaics

Wenjun Peng,[a] Jianan Wei,[a] Hongbing Li,[b] Wei Feng,[a] Mengting Liu,[a] Tianyang Xu,[a] Shudi Qiu,*[c] Chong Liu,[bf] Michael Wagner,[d] Andreas Distler,[c] Christoph J. Brabec,*[cde] Yaohua Mai*[bf] and Fei Guo*[b]

Received 8th July 2025,
Accepted 2nd October 2025

DOI: 10.1039/d5ee03888j

rsc.li/ees

Transferring the well-established perovskite ink formulations from antisolvent spin coating to scalable deposition techniques remains a great challenge, primarily owing to the strikingly different crystallization kinetics involved in the two processes. Here, we discover that a balanced trade-off between supersaturation rate and coordination capability plays an essential role in regulating the crystallization kinetics of the perovskite films deposited by scalable methods. In comparison with the commonly used DMF/DMSO solvent mixture, incorporating a small volume of NMP promotes rapid α-phase perovskite nucleation together with controllable crystal growth. Consequently, high-quality crystalline perovskite films with large grains and a void-free buried interface are readily obtained by blade coating. On these bases, inverted perovskite solar cells (0.09 cm^2) and mini-modules (21.84 cm^2) achieve high efficiencies of 25.38% and 23.22%, respectively. Furthermore, the unencapsulated solar cells deliver remarkable durability under maximum power point (MPP) tracking, maintaining 87% of their initial efficiency over 1000 h. This work provides an important avenue to bridge the gap between lab-scale cells and fab-scale perovskite photovoltaic modules.

Broader context

Scalable processing of high-performance perovskite photovoltaics is essential for realizing their commercial potential in sustainable energy technologies. Among various scalable techniques, blade coating combined with vacuum quenching showcases a promising route for large-area perovskite film deposition, owing to its compatibility with continuous manufacturing, *e.g.*, roll-to-roll printing, and its flexibility in regulating film drying kinetics. However, directly transferring well-established ink formulations developed for anti-solvent assisted spin coating often results in poor film quality under vacuum-assisted conditions due to differences in crystallization kinetics. To address this challenge, this work reveals that a balanced control of supersaturation rate and solvent coordination is critical for achieving high-quality perovskite films *via* vacuum-assisted blade coating. By judiciously incorporating *N*-methyl-2-pyrrolidone (NMP) into the ink formulation, we enable rapid nucleation and controlled crystal growth, yielding dense, large-grained, and void-free films. This strategy translates into blade coated perovskite solar cells and mini-modules with efficiencies of 25.38% and 23.22%, respectively, demonstrating its effectiveness and robustness in the upscaling of perovskite solar cells.

[a] *College of Information Science and Technology, Jinan University, Guangzhou, 510632, China*
[b] *Institute of New Energy Technology, College of Physics and Optoelectronic Engineering, Jinan University, Guangzhou, 510632, China. E-mail: yaohuamai@jnu.edu.cn, fei.guo@jnu.edu.cn*
[c] *Institute of Materials for Electronics and Energy Technology (i-MEET), Department of Materials Science and Engineering, Friedrich-Alexander-Universität Erlangen-Nürnberg, Martensstraße 7, 91058, Erlangen, Germany. E-mail: shudi.qiu@fau.de, christoph.brabec@fau.de*
[d] *Helmholtz Institute Erlangen-Nürnberg for Renewable Energy (HIERN), Forschungszentrum Jülich, Immerwahrstraße 2, 91058, Erlangen, Germany*
[e] *IMD-3, Forschungszentrum Jülich Geb. 02.6, Wilhelm-Johnen-Straße, D-52428 Jülich, Germany*
[f] *Guangdong Mellow Energy Co., Ltd, Zhuhai, 519000, China*

Introduction

Solution processing has emerged as a promising approach for scalable, cost-effective, and high-throughput manufacture of perovskite photovoltaic devices.[1–5] Currently, lab-scale perovskite solar cells (PSCs) fabricated *via* antisolvent-assisted spin coating (AASC) have achieved certified power conversion efficiencies (PCEs) exceeding 27%, on par with that of silicon solar cells.[6] With the efficiency of PSCs approaching their realistic limits, research emphases have progressively shifted from an efficiency race toward the viability of scalable production,[7,8] which is one of the essential considerations for the commercialization of

the technology. To this end, a shift of technological focus from spin coating to scalable deposition of perovskite thin-films has to be realized.[9–11] Among the few scalable methods, as an industry-compatible production technique, blade coating is widely used as a proof-of-concept for transferring the optimized perovskite recipes from small-size spin-coating to scalable production lines.[12–14] However, noticeable efficiency gaps are always observed between spin-coated PSCs and their blade-coated counterparts, with efficiencies of the latter lagging far behind.[7,15]

In comparison with spin-coating, the fundamental limitation in scalable deposition of high-quality perovskite thin-films arises from the difficulty in controlling the crystallization dynamics.[16–19] In the spin-coating process, a high supersaturation rate is facilely created by antisolvent quenching, which abruptly alters the solution state, promoting rapid nucleation and uniform grain growth.[20–22] However, antisolvent quenching is inherently incompatible with scalable coating methods due to the difficulty in solvent exchange across large-area substrates. To bypass this limitation, several quenching protocols, including vacuum quenching, gas quenching and thermal quenching, have been developed to regulate the supersaturation kinetics in a scalable deposition process.[23,24] Among them, vacuum quenching stands out for its ability to uniformly extract solvents by reducing ambient pressure, thereby controlling over supersaturation rate. In addition, decoupling of the solvent-quenching process from the precursor film deposition makes it compatible with scalable production lines.[25–27] Nevertheless, if we directly transfer the well-established perovskite ink formulations, particularly designed for spin-coating, to scalable deposition methods, it is often challenging to obtain high-quality perovskite thin-films with optoelectronic properties comparable to those prepared by AASC.

Recently, significant attention has been devoted to solvent engineering, which is closely related to the solvent evaporation dynamics in the crystallization process.[28–30] During vacuum-quenching, the wet precursor film transitions to a supersaturated state as the solvents evaporate, providing the thermodynamic driving force for nucleation and crystal growth. Hence, the supersaturation rate largely determines the density of nucleation, which in turn governs the grain size, film uniformity, and defect densities.[31,32] On the other hand, crystallization kinetics is also dictated by solvent–solute coordination of the precursor film.[33] For instance, the commonly used solvents such as dimethyl sulfoxide (DMSO) can strongly coordinate with Pb^{2+} ions *via* Lewis acid–base interactions, thereby retarding the otherwise fast crystallization.[14] However, the strongly coordinated DMSO can be trapped inside the formed intermediate phases. The DMSO rich complexes delay film formation at the perovskite/substrate region and can lead to a drying front that runs downwards from the top. Such unfavorable drying kinetics are prone to generate voids at the perovskite/substrate interface before or during the subsequent thermal annealing.[34] It is noticed that *N*-methyl-2-pyrrolidone (NMP) has been reported to form PbI_2-solvent intermediates in spin-coated perovskite films. The presence of NMP regulates crystallization during antisolvent-assisted spin coating, *via* intercalation-exchange,[35] and Lewis acid–base adduct-mediated growth and it plays a vital role in defect passivation.[36–38] In addition, the recent meniscus-assisted coating studies employing a gas knife have emphasized volatility control and limiting NMP fractions to improve large-area uniformity.[39,40] Apparently, the supersaturation rate, the coordination between the precursor solvents and the evaporation rate dynamically control nucleation and crystal growth of the perovskite films. While an in-depth understanding of the drying kinetics is on the way,[41] advanced methods to control the supersaturation rate and coordination capability as required to control film formation by ink design are still missing, which is of vital importance for realizing scalable manufacture of high-quality perovskite thin-films and solar devices.

In this work, we first identify that the perovskite ink formulations well-optimized for AASC are not transferable to scalable deposition techniques. Using supersaturation rate numerical simulations, we found that the quality of perovskite films fabricated *via* vacuum-assisted crystallization is impaired by the relatively low vacuum-quenching efficiency and the persistent entrapment of strongly coordinating solvents within the solvated intermediate phases. In light of this, we reformulated the precursor ink by introducing a small amount of NMP. This subtly decouples the DMSO-related complexes and controls crystal growth. The balanced supersaturation rate and coordination capability lead to dense, uniform, defect-less perovskite thin-films by blade coating. Perovskite solar cells (0.09 cm^2) show an impressive efficiency of 25.38%, along with a high open-circuit voltage (V_{OC}) of 1.19 V. Meanwhile, a mini-module with an aperture area of 21.84 cm^2 achieves a PCE of 23.22%.

Results and discussion

Tailoring solvent composition for vacuum-quenching-assisted blade-coating

We start with the investigation of directly transferring the state-of-the-art efficient perovskite ink, well-established for AASC protocols, to scalable VABC. As illustrated in Fig. 1a, perovskite films were prepared by AASC and VABC using the identical ink formulation of $FA_{0.85}MA_{0.1}Cs_{0.05}PbI_3$ dissolved in DMF/DMSO (4/1, v/v). During the spin-coating process, antisolvent dripping usually takes place a few seconds before the substrate spin stops. At that moment, the residual solvent of the precursor film is instantly extracted, thereby inducing an ultra-high supersaturation rate that drives fast crystallization. In contrast, blade-coating results in a wet perovskite precursor film full of solvent that is subsequently subjected to vacuum pumping. In this step, the solvent evaporates more slowly compared to antisolvent dripping, which increases the risk of residual solvent entrapment within the intermediate films. Fig. 1b and c show the scanning electron microscopy (SEM) images of the perovskite films prepared by AASC and VABC, respectively. It is seen that AASC yields a dense and compact perovskite film, whereas the film produced *via* VABC consists of larger grains with a number of voids, leading to incomplete surface coverage. Not

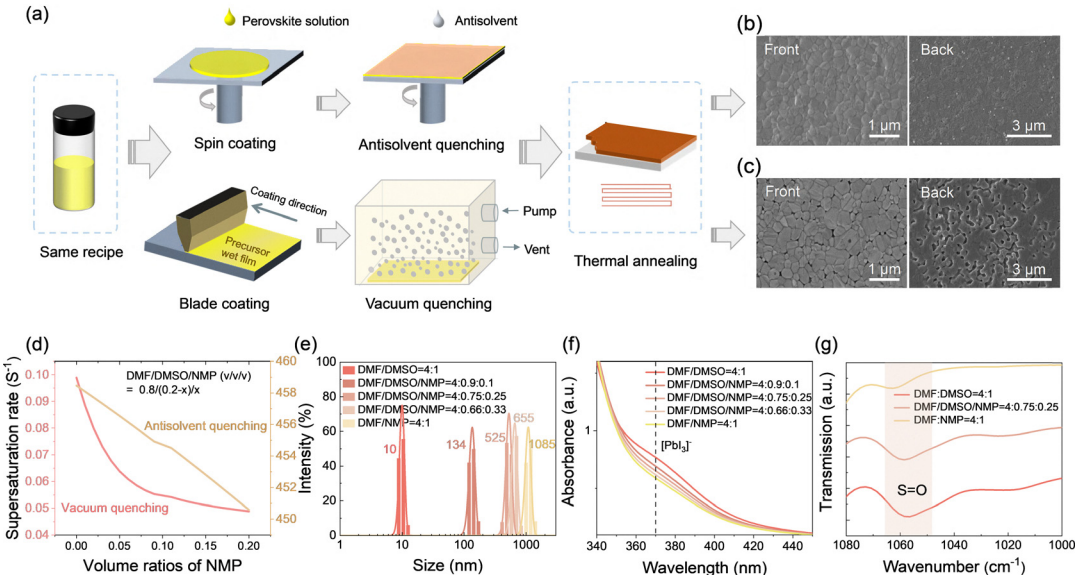

Fig. 1 (a) Schematic illustration of the vacuum quenching-assisted blade coating (VABC) and antisolvent-assisted spin coating (AASC) process. Top-view SEM images of the top surface and the back surface peeled from the perovskite/substrate bottom interfaces of films prepared by (b) AASC and (c) VABC. (d) Calculated supersaturation rate at the critical concentration for the DMF/DMSO/NMP solvent system with the antisolvent quenching and vacuum quenching method. (e) Colloidal size distribution of the perovskite precursor solution in various DMF/DMSO systems after the addition of NMP, with the volume ratio relative to DMSO. (f) UV-vis absorption spectra of PbI_2 dissolved in DMF/DMSO with varying NMP volumes. (g) FTIR spectra of the intermediate powders obtained by vacuum-quenching, which were processed from DMF/DMSO, DMF/NMP, and DMF/DMSO/NMP.

surprisingly, when the perovskite films were peeled off from the substrates, the buried interface of the AASC-processed film remains dense and uniform, while the VABC-processed film reveals noticeable discontinuous voids. The formation of these voids in the VABC-processed film can be ascribed to the fact that the residual DMSO is trapped within the intermediate film during vacuum extraction and is rapidly removed by thermal annealing.[42] These morphological deficiencies directly correlate with the inferior photovoltaic performance of the blade-coated solar cells compared to their spin-coated counterparts. As shown in Fig. S1 and S2, the AASC-based solar cells give an average power conversion efficiency (PCE) of 24.06%, whereas the VABC-based solar cells exhibit a lower average PCE of 19.94%, mainly due to the marked reduction in short-circuit current density (J_{SC}), open-circuit voltage (V_{OC}), and fill factor (FF).

To elucidate the reason behind this, we calculated the supersaturation rates of perovskite precursors dissolved in the same DMF/DMSO (4/1, v/v) solvent system but with different quenching methods (Fig. S3).[23] It is found that antisolvent quenching induces a supersaturation rate of $\sim$458.46 s^{-1}, whereas vacuum quenching results in a significantly lower supersaturation rate of $\sim$0.09 s^{-1}. A similar trend is observed in the commonly reported DMF/NMP (4/1, v/v) solvent system, which is widely used for gas-quenching assisted blade coating (Fig. S3). These results suggest that antisolvent quenching is substantially faster to create supersaturation compared to vacuum-quenching. Hence, the ink formulations optimized for AASC are not transferable to VABC, emphasizing the importance of solvent reformulation in tailoring crystallization pathways for different crystallization protocols.

In this context, in order to modulate the crystallization kinetics of perovskites deposited by VABC to achieve desired film morphology, we reformulate the solvent system by introducing small volumes of NMP (x) to the conventional solvent mixture of DMF/DMSO (v/v = $4/(1 - x)$). The selection of NMP is mainly because of its low saturated vapor pressure along with a lower coordination capability for PbI_2 compared to that of DMSO (Table S1, SI).[43] Fig. 1d shows that as the fraction of NMP in DMSO increases, the supersaturation rate decreases significantly during vacuum quenching, which suggests that NMP is more slowly removed than DMSO during vacuum quenching. A similar trend is observed even in the antisolvent-assisted quenching process with high quenching efficiency.

We hence evaluate the critical role of NMP in forming colloidal complexes in perovskite precursor solutions. The solubility of lead iodide (PbI_2) powder is first examined in solvents DMSO, NMP, and DMSO/NMP. As shown in Fig. S4, a DMSO-based solution appears more transparent compared to NMP and DMSO/NMP mixtures, indicating that the strong coordination between DMSO and PbI_2 stabilizes the precursor solution and enhances its solubility. The colloidal size distribution of PbI_2 dissolved in the various solvent mixtures was analyzed using dynamic light scattering (DLS) (Fig. 1e). DMF/DMSO yields a colloidal particle size of around 10 nm. Upon addition of 10 vol% NMP (relative to DMSO), the size increases to $\sim$134 nm. When DMSO is entirely replaced by NMP, the colloidal size further increases to $\sim$1085 nm, which is markedly larger than that of the DMF/DMSO system. The enlarged colloidal particles can be ascribed to the formation of large

NMP–PbI_2 complexes due to NMP molecules being larger than DMSO molecules, which promote aggregation and thus reduce precursor solubility. The UV-vis absorption spectra shown in Fig. 1f demonstrate a decrease in the absorption characteristic peak of $[PbI_3]^-$ at 370 nm, suggesting the reduced complexation of PbI_2 with DMSO in the presence of NMP. Additionally, Fourier transform infrared (FTIR) spectra (Fig. 1g) show a shift in the S=O bond peak in the presence of NMP, indicating that NMP containing C=O groups could further reduce the coordination of DMSO–PbI_2. Given that the formation of solute–solvent complexes in the precursor solution can profoundly impact the crystallization process,[18] we anticipate that the introduction of NMP into the DMF/DMSO solvent mixture would significantly modulate the crystallization kinetics of perovskite films deposited by VABC.

Crystallization kinetics of the perovskites by the VABC

Given the importance of the vacuum-quenching process in the formation of intermediate adducts, we first carried out X-ray diffraction (XRD) to analyze the composition of the intermediate films obtained from the vacuum quenching. It is seen that the intermediate film processed from DMF/DMSO (4/1, v/v) contains a significant amount of solvent-coordinated complexes, as indicated by the characteristic diffraction peaks at 9.3° associated with DMSO adduct intermediates (Fig. 2a).[35] For the DMF/NMP (4/1, v/v) solvent system, a distinct diffraction

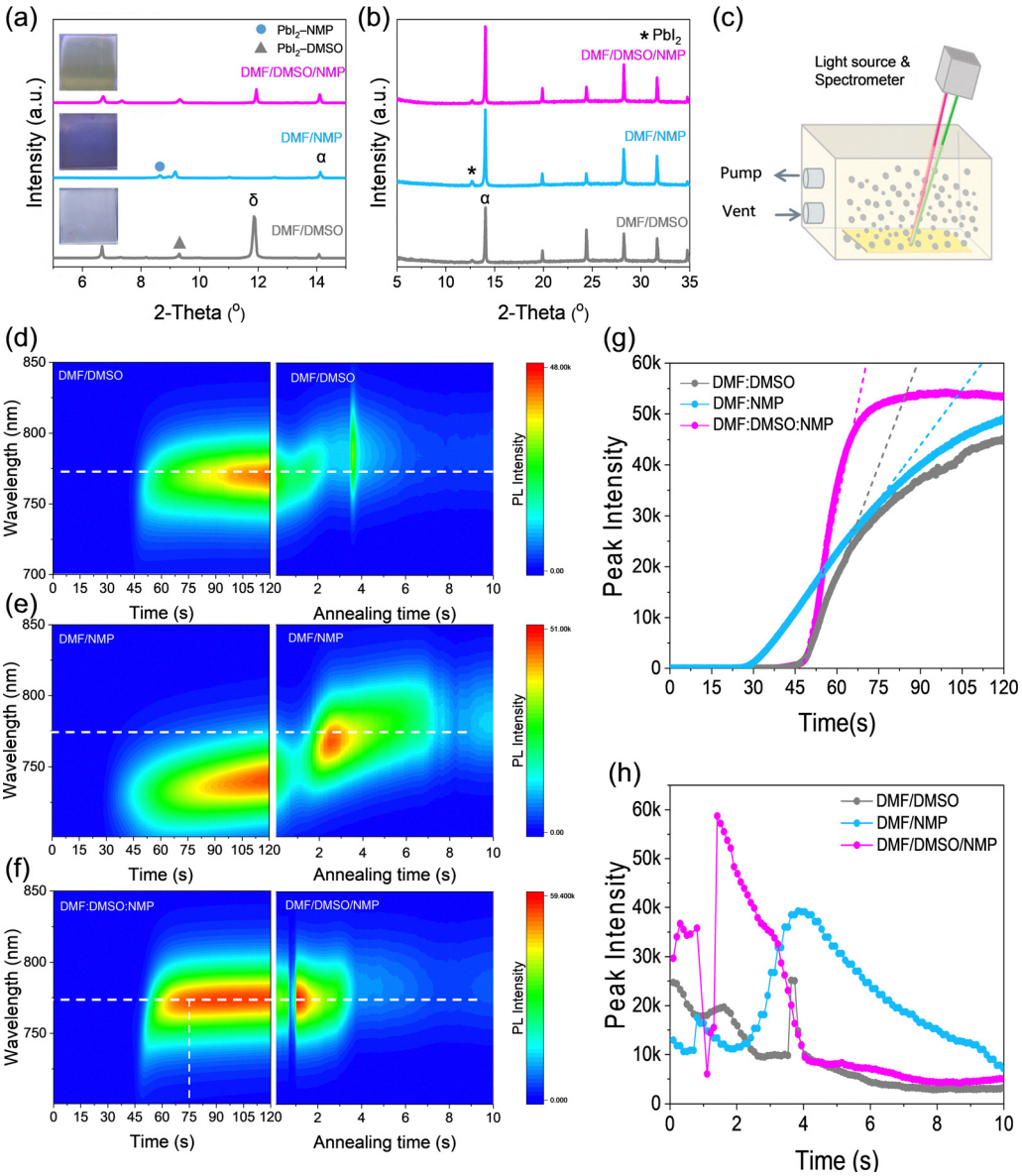

Fig. 2 (a) XRD patterns of the prepared intermediate films after vacuum quenching. (b) XRD patterns of the perovskite films after thermal annealing. (c) Schematic illustration of the vacuum quenching setup integrated with an *in situ* optical monitor unit. Photoluminescence (PL) spectra evolution during the vacuum quenching stage (left) and thermal annealing process (right) for perovskite films blade-deposited from the three solvent systems: (d) DMF/DMSO, (e) DMF/NMP and (f) DMF/DMSO/NMP. Evolution of the PL peak intensity of the three films during (g) vacuuming and (h) the annealing process.

peak at $2\theta = 8.6^\circ$ is observed, signifying the formation of NMP-related complexes.[44] The presence of these complexes suggests that NMP interacts with PbI_2, though likely with a weaker interaction strength, stabilizing the intermediate phase. In contrast, replacing 1/4 volume of DMSO with NMP, the film deposited from the ternary solvent DMF/DMSO/NMP (4/0.75/0.25, v/v/v) exhibits a suppression of all solvent-related characteristic peaks. This indicates that the inclusion of NMP effectively disrupts excessive DMSO–PbI_2 complex formation, facilitating a more efficient solvent removal process. Additionally, all the three intermediate films exhibit diffraction peaks at $2\theta = 14^\circ$, suggesting the formation of the α-phase perovskite. We note that the δ-phase observed in the DMSO-based film, other than the DMF/NMP-based film, suggests DMSO's tendency to induce a yellow δ-phase in the FA-based perovskite. The XRD pattern of the intermediate films after one hour in the air, shown in Fig. S5, reveals that the incorporation of a small amount of NMP can inhibit the δ-phase perovskite formation. Changes of intermediate films in air for one hour indicate great environmental stability of the ternary-solvent-based film, which is highly beneficial for scalable production owing to extended processing windows (Fig. S6). Fig. 2b displays the XRD patterns of the crystallized perovskite films after thermal annealing. All films exhibit characteristic perovskite diffraction peaks, with the (100) peak at 14° being the most prominent. In contrast to the DMF/DMSO-based film, which exhibits broader peaks with lower intensity, the DMF/DMSO/NMP-based films display intense (100) peaks with smaller full-width at half maximum (Fig. S7), indicating larger crystal grains with reduced lattice disorder.[2] The DMF/NMP-based film, however, exhibits a clear PbI_2 peak at 12.7°, whereas this peak is significantly suppressed in the case of the DMF/DMSO/NMP-based film (Fig. S8). We attribute this to the high boiling point of NMP, which causes its slow release during annealing and consequently promotes the formation of PbI_2. This finding is corroborated by SEM analysis, which shows dendrite-like crystals and non-uniform morphology in the DMF/NMP-based film (Fig. 3b), in contrast to the more compact morphology observed for the DMF/DMSO/NMP-based film.

To unveil the critical role of NMP in regulating the crystallization kinetics of the perovskite film formation by VABC, we carried out *in-situ* photoluminescence (PL) to monitor the

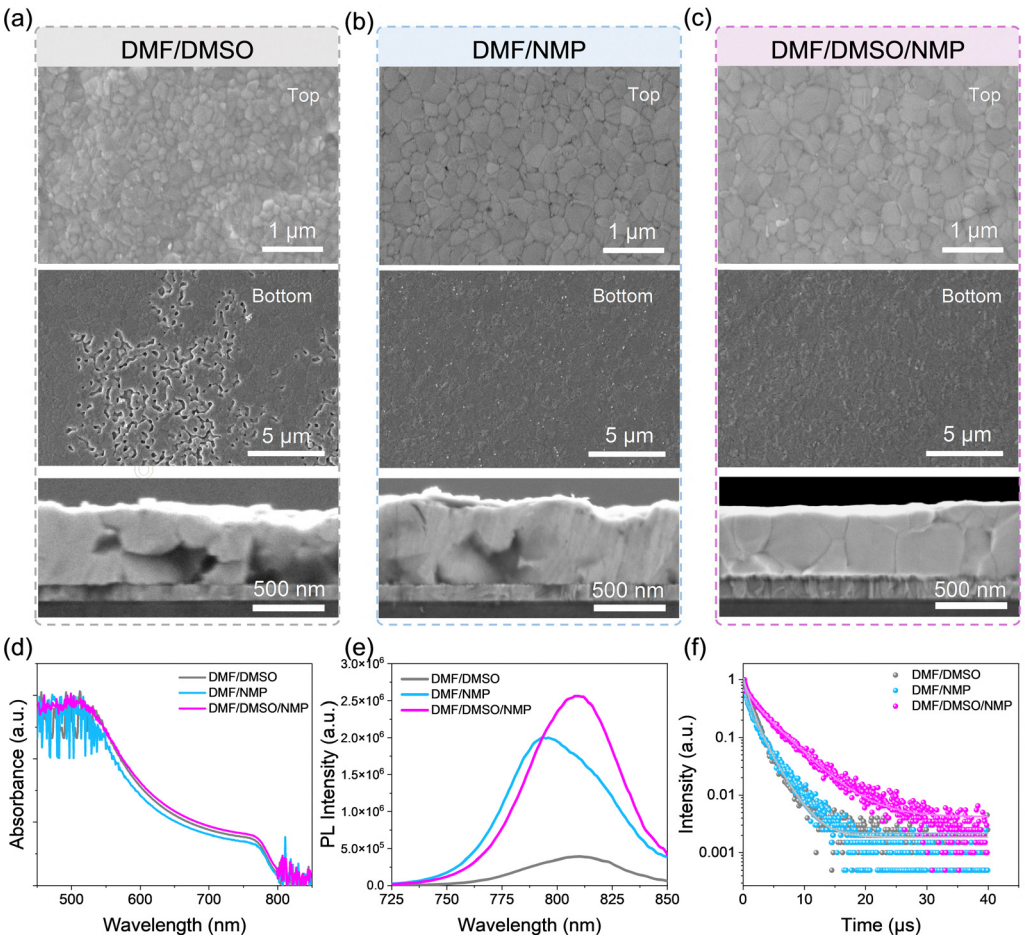

Fig. 3 SEM images of perovskite films processed from DMF/DMSO (a), DMF/NMP (b), and DMF/DMSO/NMP (c) solvent systems (top panel: top surface, middle panel: buried interface; and bottom panel: cross section). (d) UV-vis absorption, (e) steady-state PL and (f) TRPL spectra of the perovskite films processed from the three solvent systems by VABC.

drying process, as illustrated in Fig. 2c. Fig. 2d–f show the PL evolution plots of the as-bladed wet precursor film during the implementation of vacuum quenching for 120 s, followed by a thermal annealing at 100 °C for 10 s. The corresponding PL peak intensities are extracted and shown in Fig. 2g and h. The first detectable PL peaks emerge at around 45 s of the vacuum quenching for the two films containing DMSO, whereas it occurs earlier (~30 s) for the DMF/NMP system. The accelerated PL onset suggests that NMP promotes nucleation of the α-phase perovskite. Notably, the integrated PL intensity for the DMF/NMP system increases gradually from 30 to 120 s (Fig. 2g). The DMF/DMSO system exhibits a rapid increase in PL intensity between 45 and 65 s, followed by a slower rise up to the end of vacuum quenching. In striking contrast, the PL intensity of the ternary solvent system reaches a plateau with the highest intensity at 75 s, maintained until 120 s. The extracted PL peak positions, as shown in Fig. S9a and b, clearly show a PL redshift during the initial 75 s, after which the PL signals stabilize at distinct wavelengths of approximately 775, 770, and 730 nm for the DMF/DMSO, DMF/DMSO/NMP, and DMF/NMP systems, respectively. These observations suggest that nucleation predominantly takes place during the first 75 s of vacuum treatment. It can be rationalized that rapid evaporation of DMF drives the precursor wet film toward supersaturation, while the comparatively weak coordinating ability of NMP, relative to DMSO, promotes the interaction between PbI_2 and cationic salts, thereby accelerating the nucleation process. Subsequently, between 75 and 120 s of the vacuum quenching, the relatively low volatility of NMP, attributed to its lower saturated vapor pressure, leads to slow and controllable crystal growth. On the other hand, the stronger coordination and higher volatility of DMSO increase the risk of solvent entrapment within the film because of the uneven evaporation of the precursor wet film at its interface and bulk.

When the intermediate films are subjected to thermal annealing at 100 °C, distinctively different crystal growth behaviors are observed as well (Fig. 2d–f). The DMF/DMSO-based film exhibits a pronounced PL intensity peak at 3.5 s, likely attributed to the rapid release of residual DMSO. In the case of the DMF/NMP-based film, PL intensity shows a slow increase from 2 to 4 s, followed by a steady decline. Simultaneously, the PL peak position redshifts gradually from 730 nm to 780 nm over the whole period of annealing due to slow NMP release. By contrast, the ternary DMF/DMSO/NMP system displays a continuous and smooth decrease in PL intensity along with a redshift to 780 nm in the first 4 s, showcasing a more stable and controlled crystallization pathway. Overall, the introduction of NMP effectively balances supersaturation kinetics and solvent coordination, enabling rapid nucleation and well-controlled crystal growth.

These crystallization pathways can be rationalized using the classical LaMer model (Fig. S10). In the DMF/DMSO system, rapid supersaturation driven DMF and free DMSO evaporation leads to an overshoot in nucleation density. Once the solute concentration drops below the critical value C^*_{min}, the system enters a diffusion-controlled growth regime, where rapid crystal growth at the liquid–vapor interface results in the formation of a dense capping-layer. This blocking layer traps residual DMSO within the intermediate film, which is later expelled during annealing, leading to voids at the buried interface (Fig. S11).[14] Conversely, the ternary solvent DMF/DMSO/NMP suppresses excessive nucleation to reduce the formation of the blocking layer and mitigates the solvent entrapment. We therefore conclude that the incorporation of NMP balances supersaturation kinetics and solvent coordination by virtue of its lower donor number and reduced vapor pressure, offering a more controllable crystallization pathway conducive to the formation of dense, high-quality perovskite films.[45]

Impact of the solvent composition on film quality

The distinctly different crystallization kinetics observed in the three solvent systems are expected to profoundly impact the resulting film morphology and optoelectronic properties. Fig. 3a–c show the SEM images of the crystalline perovskite films from the view of top surface (top), buried interface (middle) and cross section (bottom). It is evident that the perovskite film processed from DMF/DMSO is composed of small crystals with an average grain size of 183.9 nm (Fig. 3a and Fig. S12). The formation of small crystals can be attributed to the rapid volatilization of free DMF that drives extensive nucleation, which also leads to high surface roughness and height variations (Fig. 3a). In striking contrast, the DMF/NMP-based film shows significantly larger crystals with an average grain size of 478.1 nm (Fig. 3b and Fig. S12). The enlarged crystals with reduced surface roughness can be ascribed to the retarded nucleation rate together with controllable grain growth, as a result of the slower evaporation rate of NMP. In addition, the DMF/DMSO/NMP-based film exhibits an average crystal grain size of 446.9 nm and, in parallel, the most uniform and compact morphology (Fig. 3c). The differences in surface morphology are further evident in the atomic force microscopy (AFM) images (Fig. S13).

The different crystallization kinetics of the perovskite films prepared by VABC also lead to dramatically different crystal morphology at the buried interface (Fig. S14). For perovskite films processed from DMF/DMSO, the fast crystallization along with the presence of trapped residual DMSO by vacuum-quenching results in the formation of a large number of voids at the buried interface after thermal annealing (Fig. 3a). Such severe morphological defects can lead to incomplete contact with the underlying interface layer, thereby compromising the extraction of photon generated charge carriers.[46] In contrast, the NMP-involved films exhibit fully covered and void-free buried interfaces (Fig. 3a and c), which can be ascribed to retarded crystal growth owing to their moderate coordination and slow volatilization.

UV-vis absorption spectra of the three perovskite films are plotted in Fig. 3d. Due to the presence of a large number of voids, the DMF/DMSO-based film exhibits the lowest light absorption. In contrast, the DMF/NMP-processed film exhibits enhanced absorption across the entire wavelength range, attributed to its void-free morphology. The highest absorption intensity

is observed for the DMF/DMSO/NMP-based film, mainly owing to its compact crystal along with improved crystallinity. Fig. 3e depicts the steady-state photoluminescence (PL) spectra of the bladed perovskite films. Not surprisingly, the DMF/DMOS-based film exhibits the weakest emission intensity owing to the presence of a high density of defects. In comparison, the DMF/DMSO/NMP-based film exhibits the highest PL intensity, centering at 810 nm, indicating a significant suppression of defect-induced nonradiative recombination. We further performed time-resolved photoluminescence (TRPL) measurements to estimate carrier lifetimes (Fig. 3f). The calculated average carrier lifetime (τ_{avg}) of the DMF/DMSO/NMP-based perovskite film is 3.78 μs, which is more than two times higher than those of the DMF/DMSO- and DMF/NMP-based films, 1.71 and 1.72 μs, respectively (Table S2). This prolonged carrier lifetime suggests a lower defect density and suppressed trap-assisted recombination.

Photovoltaic performance of the solar devices

We turn to investigating the photovoltaic performance of p–i–n PSCs with a device architecture of ITO/NiO_x/(4-(2,7-dibromo-9,9-dimethylacridin-10(9*H*)-yl)butyl)phosphonic acid (DMACPA)/perovskite/piperazine dihydriodide (PDI)/C_{60}/SnO_2/Cu (Fig. 4a). To find out the optimal NMP content, we prepared solar devices with perovskite films processed with varied DMF/DMSO/NMP volume ratios. The statistical photovoltaic parameters of the prepared PSCs are summarized in Fig. 4b and Fig. S15. The ternary solvent with a DMF/DMSO/NMP volume ratio of 4/0.75/0.25 yields the highest average PCE of 24.48 ± 0.9%, along with a V_{OC} of 1.18 ± 0.1 V, a J_{SC} of 25 ± 0.5 mA cm^{-2}, and an FF of 82 ± 2%. Such improvements are attributed to enhanced film morphology and crystallinity enabled by the balanced solvent coordination and evaporation kinetics. In contrast, the lowest average J_{SC} of 24.1 mA cm^{-2} is obtained for the devices fabricated using the DMF/DMSO binary solvent (v/v, 4/1). This reduction aligns with SEM results that revealed small grain sizes and high grain boundary density, both of which introduce recombination centers and hinder charge transport, ultimately compromising photocurrent and device efficiency.

Current density–voltage (*J–V*) curves of the champion devices for each condition are shown in Fig. 4c and Fig. S16, with the corresponding PV parameters tabulated in Table 1 and Table S3. The DMF/DMSO/NMP-based device achieves an outstanding PCE of 25.38%, along with a J_{SC} of 25.57 mA cm^{-2}, a V_{OC} of 1.19 V, and an FF of 83.69%. These metrics substantially surpass those of the DMF/DMSO-based (21.24%) and DMF/NMP-based (22.72%) devices. The integrated photocurrent densities derived from the external quantum efficiency (EQE) spectra (Fig. 4d) are 23.23, 23.71, and 25.04 mA cm^{-2} for the DMF/DMSO, DMF/NMP, and DMF/DMSO/NMP-based devices, respectively, which are in excellent agreement with the J_{SC} values from the *J–V* measurements. To verify the reliability of our *J–V* measurement, we sent one of our best-performing devices to Prof. Xianzhong Lin's lab in Sun Yat-sen University for third-party testing. The solar cell gives a high PCE of 25.12% (reverse scan) along with a V_{OC} of 1.17 V (Fig. S17). Stabilized power output (SPO) under continuous AM 1.5G illumination at the maximum power point (MPP) (Fig. 4e) further confirms the reliability of enhanced performance. The DMF/DMSO/NMP-based solar cell maintains a steady J_{SC} of 24.89 mA cm^{-2} and an SPO of 24.61%, highlighting superior operational stability.

To better understand the origins of the enhanced photovoltaic performance of the ternary-solvent-based device, we carried out comprehensive optoelectronic characterization

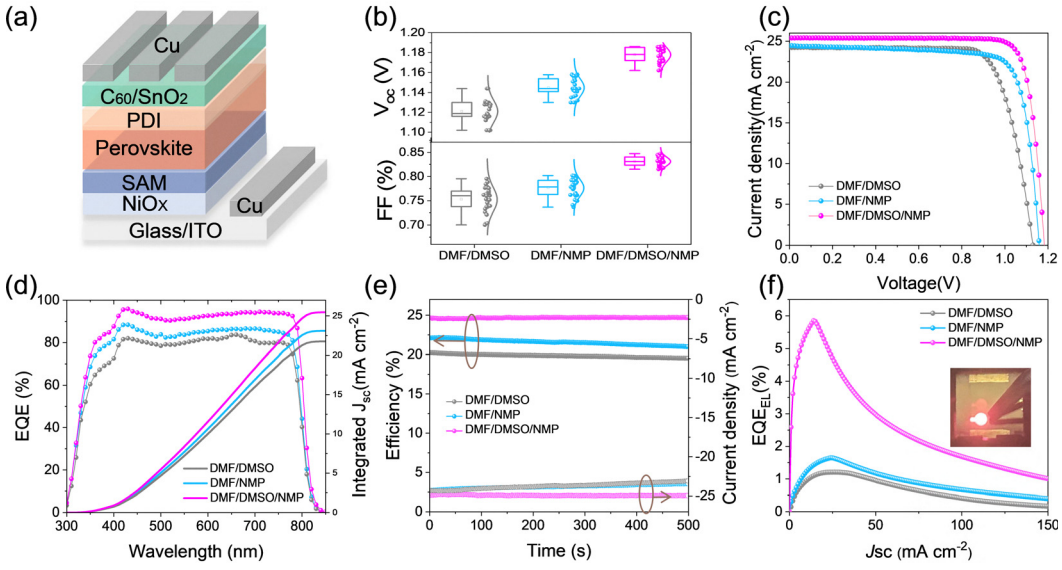

Fig. 4 (a) Schematic illustration of the device architecture. (b) Statistical distribution of PCE for PSCs fabricated using DMF/DMSO, DMF/NMP, and DMF/DMSO/NMP solvent systems. (c) *J–V* curves of PSCs processed with the three typical solvent systems. (d) External quantum efficiency (EQE) spectrum and the corresponding integrated J_{SC}. (e) Steady-state power output of the champion solar cells. (f) Corresponding external quantum efficiency of electroluminescence (EQE_{EL}) as a function of current.

Table 1 Photovoltaic parameters of the PSCs processed from the three solvent systems

Sample	V_{OC} (V)	J_{SC} (mA cm^{-2})	FF (%)	PCE (%)
DMF/DMSO	1.13	24.28	77.43	21.24
DMF/NMP	1.16	25.04	78.37	22.72
DMF/DMSO/NMP	1.19	25.57	83.69	25.38

studies. As shown in the dark *J–V* curves (Fig. S18), the DMF/DMSO/NMP device exhibits markedly lower reverse leakage current, giving rise to a higher rectification ratio, which is beneficial for charge transport within the device. Light intensity-dependent V_{OC} measurements are shown in Fig. S19. DMF/DMSO- and DMF/NMP-based PSCs exhibit ideality factors (n) of 1.72 and 1.52, respectively. In contrast, the DMF/DMSO/NMP-based device shows a reduced n of 1.43, confirming suppressed trap-associated recombination. Electrochemical impedance spectroscopy (EIS) spectra shown in Fig. S20 reveal a progressive increase in recombination resistance (R_{rec}) from DMF/DMSO- to DMF/NMP-based devices, reaching a maximum for the DMF/DMSO/NMP-based device. Transient photovoltage (TPV) measurements (Fig. S21) further attest that the DMF/DMSO/NMP device exhibits the longest carrier lifetime, consistent with the minimized non-radiative recombination and optimized charge transport. A good solar cell should also be a good light-emitting diode (LED). We thus measured the external quantum efficiency of electroluminescence (EQE_{EL}) of the solar devices functioning as LEDs under forward bias in the dark. As shown in Fig. 4f, the EQE_{EL} values obtained under driving current densities equivalent to their J_{SC} values of the DMF/DMSO-, DMF/NMP-, and DMF/DMSO/NMP-based devices are 1.20%, 1.63%, and 4.71% respectively, giving the nonradiative V_{OC} losses of 115, 107 and 79 mV (Table S4).

Scalability and stability evaluation

To demonstrate the scalability of the solvent-tailoring protocol for VABC, we fabricated perovskite solar mini-modules based on the optimized DMF/DMSO/NMP solvent system. Firstly, a 3-subcell mini-module with an aperture area of 2.05 cm^2 was prepared, giving a PCE of 24.12%, along with a J_{SC} of 8.44 mA cm^{-2}, an FF of 80.49% and a V_{OC} of 3.55 V (Fig. S22), presenting a marginal efficiency drop as compared to the small-size cell. We then fabricated a larger 7-subcell mini-module with an aperture area of 21.84 cm^2 (schematic shown in Fig. 5a), which yields an impressive PCE of 23.22%, along with a J_{SC} of 3.08 mA cm^{-2}, an FF of 80.27% and a V_{OC} of 8.07 V (Fig. 5c). In addition, the module shows negligible hysteresis, which can be attributed to the suppressed ion migration. A comparison of the efficiency loss of the devices during upscaling with previous reports demonstrates that our blade-coated devices exhibit the lowest efficiency decline as the aperture area increases from 0.09 cm^2 to 21.84 cm^2, corresponding to a small efficiency loss of 2.16% (Fig. 5d). These results attest to the high-quality perovskite thin films obtained by VABC over large areas.

Lastly, we evaluated the stability of the blade-coated PSCs. Fig. 5e shows the shelf stability of the unencapsulated devices stored in an N_2-filled glovebox. It is seen that the PCEs of the DMF/NMP- and DMF/DMSO-based devices drop to 58% and 47% of their initial values after 2000 hours of storage, respectively. Noticeably, the DMF/DMSO/NMP-based solar

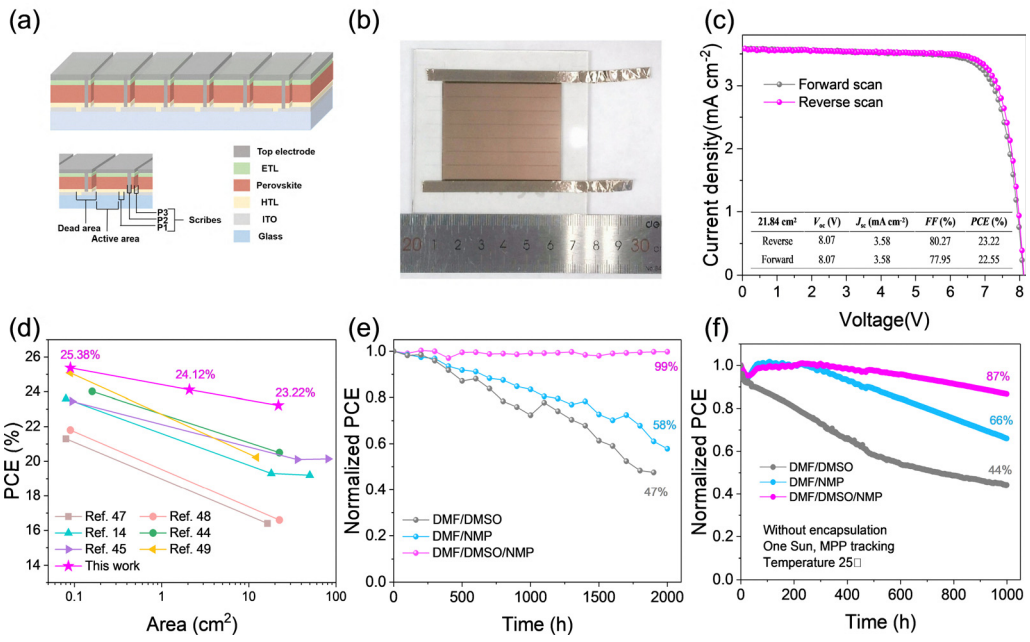

Fig. 5 (a) Schematic diagram of the perovskite mini-module. (b) Digital photograph and (c) *J–V* curves of the best-performing mini-module on a 7.6 cm × 7.6 cm substrate based on the DMF/DMSO/NMP solvent system. (d) Comparison of the efficiency decline during upscaling of the present work with those previously reported in the literature.[14,44,45,47–49] (e) Evolution of *PCE* of the unencapsulated blade-coated PSCs in an N_2-filled glove box. (f) MPP tracking of PSCs under one sun illumination.

device almost retains its original efficiency. We also examined the shelf stability of the devices in ambient air with around 50% relative humidity. As shown in Fig. S23, the DMF/DMSO/NMP-based device maintains 90% of its initial PCE after 1000 hours, which is significantly higher than those of the DMF/DMSO- (59%) and DMF/NMP-based devices (73%). Finally, the operational stability of the unencapsulated DMF/DMSO/NMP-based devices was examined under continuous maximum power point tracking (Fig. 5f), where the device maintained 87% of its initial PCE under nitrogen after 1000 hours. These results demonstrate that our tailored solvent engineering not only enhances device efficiency but also ensures superior long-term operational stability.

Conclusion

In summary, we have demonstrated the importance of modulating the supersaturation rate and coordination capability for achieving controllable crystallization kinetics for scalable deposition of high-quality perovskite thin-films. By incorporating a small amount of NMP into the widely used DMF/DMSO solvent mixture, we obtained perovskite films with a large grain size and low defect density, which are void-free at the perovskite/substrate interface, *via* vacuum-assisted blade coating. Consequently, the prepared PSCs with an active area of 0.09 cm^2 yield a champion PCE of 25.38% with excellent operational stability. The scaled-up mini modules with active areas of 2.05 cm^2 and 21.84 cm^2 deliver impressive efficiencies of 24.12% and 23.22%, respectively. These results demonstrate a substantially reduced performance gap between modules and lab-scale devices, highlighting the great potential of the solvent tailoring approach in formulating perovskite inks towards the commercialization of perovskite solar technology.

Author contributions

W. P. and J. W. conceived the idea. W. P., J. W., F. G. and S. Q. designed the project. S. Q., C. J. B., Y. M., and F. G. supervised the work. W. P. fabricated single-junction perovskite solar cells and modules. W. P. performed the optical and electrical characterization studies. S. Q., M. W. and A. D. performed supersaturation rate simulation and contributed to the optical data analysis. W. F. and H. L. obtained the SEM images. M. L. and T. X. helped perform AFM measurements. H. L. helped monitor the operational stability. W. P., S. Q., J. W., H. L., W. F. and M. L. provided valuable assistance in data analysis. F. G., C. J. B., Y. M. and C. L. provided the equipment support for the characterization. W. P. wrote the first draft of the manuscript. S. Q., A. D., M. W., F. G., and C. J. B. revised the manuscript. All the authors revised and approved the manuscript.

Conflicts of interest

The authors declare no conflict of interest.

Data availability

The data supporting this article have been included as part of the supplementary information (SI). Supplementary information is available. See DOI: https://doi.org/10.1039/d5ee03888j.

Acknowledgements

The authors acknowledge financial support from the National Natural Science Foundation of China (62174069) and Deutsche Forschungsgemeinschaft (DFG) *via* the Perovskite SPP2196 programme (Project no. 506698391). C. J. B. acknowledges funding from DFG under CRC ChemPrint. The authors further acknowledge financial support from the National Natural Science Foundation of China (M-0515). S. Q. gratefully acknowledges financial support from the China Scholarship (CSC).

References

1 K. H. Hendriks, J. J. van Franeker, B. J. Bruijnaers, J. A. Anta, M. M. Wienk and R. A. J. Janssen, *J. Mater. Chem. A*, 2017, **5**, 2346–2354.
2 Y. Zhang, X. Sun, Z. Guan, D. Li, Q. Wang, Y. Yue, F. Liu, J. Wei and H. Li, *Small Methods*, 2024, **9**, 2400214.
3 R. Wang, J. Zhu, J. You, H. Huang, Y. Yang, R. Chen, J. Wang, Y. Xu, Z. Gao, J. Chen, B. Xu, B. Wang, C. Chen, D. Zhao and W.-H. Zhang, *Energy Environ. Sci.*, 2024, **17**, 2662–2669.
4 Y. Ju, S. Y. Park, K. M. Yeom, J. H. Noh and H. S. Jung, *ACS Appl. Mater.*, 2019, **11**, 11537–11544.
5 S. Qiu, L. Dong, D. Jang, F. Yang, J. G. Cerrillo, C. Li, Z. Xie, J. Luo, F. Guo, A. Distler, T. Du, C. J. Brabec and H.-J. Egelhaaf, *Adv. Energy Mater.*, 2024, **14**, 2402616.
6 J. Du, J. Chen, B. Ouyang, A. Sun, C. Tian, R. Zhuang, C. Chen, S. Liu, Q. Chen, Z. Li, X. Wu, J. Cai, Y. Zhao, R. Li, T. Xue, T. Cen, K. Zhao and C.-C. Chen, *Energy Environ. Sci.*, 2025, **18**, 3196–3210.
7 Z. Li, T. R. Klein, D. H. Kim, M. Yang, J. J. Berry, M. F. A. M. van Hest and K. Zhu, *Nat. Rev. Mater.*, 2018, **3**, 18017.
8 F. Yang, D. Jang, L. Dong, S. Qiu, A. Distler, N. Li, C. J. Brabec and H.-J. Egelhaaf, *Adv. Energy Mater.*, 2021, **11**, 2101973.
9 X. Dai, Y. Deng, C. H. Van Brackle and J. Huang, *Int. J. Extreme Manuf.*, 2019, **1**, 022004.
10 J. W. Yoo, J. Jang, U. Kim, Y. Lee, S.-G. Ji, E. Noh, S. Hong, M. Choi and S. I. Seok, *Joule*, 2021, **5**, 2420–2436.
11 N.-G. Park and K. Zhu, *Nat. Rev. Mater.*, 2020, **5**, 333–350.
12 W. Feng, J. Tao, G. Liu, G. Yang, J. X. Zhong, Y. Fang, L. Gong, S. Yang and W.-Q. Wu, *Angew. Chem., Int. Ed.*, 2023, **62**, 202300265.
13 K. Liu, Q. Liang, M. Qin, D. Shen, H. Yin, Z. Ren, Y. Zhang, H. Zhang, P. W. K. Fong, Z. Wu, J. Huang, J. Hao, Z. Zheng, S. K. So, C.-S. Lee, X. Lu and G. Li, *Joule*, 2020, **4**, 2404–2425.
14 S. Chen, X. Dai, S. Xu, H. Jiao, L. Zhao and J. Huang, *Science*, 2021, **373**, 902–907.

15 C. Huang, S. Tan, B. Yu, Y. Li, J. Shi, H. Wu, Y. Luo, D. Li and Q. Meng, *Joule*, 2024, **8**, 2539–2553.
16 Z. Li, X. Liu, C. Zuo, W. Yang and X. Fang, *Adv. Mater.*, 2021, **33**, 2103010.
17 D. Liu, W. Zhou, H. Tang, P. Fu and Z. Ning, *Sci. China Chem.*, 2018, **61**, 1278–1284.
18 Q. Gao, J. Qi, K. Chen, M. Xia, Y. Hu, A. Mei and H. Han, *Adv. Mater.*, 2022, **34**, 2200720.
19 I. A. Howard, T. Abzieher, I. M. Hossain, H. Eggers, F. Schackmar, S. Ternes, B. S. Richards, U. Lemmer and U. W. Paetzold, *Adv. Mater.*, 2019, **31**, 1806702.
20 W. R. Wu, C. J. Su, W. T. Chuang, Y. C. Huang, P. W. Yang, P. C. Lin, C. Y. Chen, T. Y. Yang, A. C. Su, K.-H. Wei, C.-M. Liu and U.-S. Jeng, *Adv. Energy Mater.*, 2017, **7**, 1601842.
21 Y. Yan, Y. Yang, M. Liang, M. Abdellah, T. Pullerits, K. Zheng and Z. Liang, *Nat. Commun.*, 2021, **12**, 6603.
22 H. Shim, J.-H. Park, S. Choi and C.-J. Kim, *Curr. Appl. Phys.*, 2024, **66**, 60–65.
23 S. Ternes, F. Laufer and U. W. Paetzold, *Adv. Sci.*, 2024, **11**, 2308901.
24 H. Lai, J. Hu, X. Zhou, L. Cai, Q. He, C. Chen, Z. Xu, X. Xiao, D. Lan, Y. Mai and F. Guo, *Solar RRL*, 2022, **6**, 2200619.
25 D. Liu, X. Jiang, H. Wang, H. Chen, Y. B. Lu, S. Dong, Z. Ning, Y. Wang, Z. Wu and Z. Ling, *Adv. Sci.*, 2024, **11**, 2400150.
26 F. Guo, W. He, S. Qiu, C. Wang, X. Liu, K. Forberich, C. J. Brabec and Y. Mai, *Adv. Funct. Mater.*, 2019, **29**, 1900964.
27 Z. Wang, Y. Lu, Z. Xu, J. Hu, Y. Chen, C. Zhang, Y. Wang, F. Guo and Y. Mai, *Adv. Sci.*, 2021, **8**, 2101856.
28 E. Rezaee, W. Zhang and S. R. P. Silva, *Small*, 2021, **17**, 2008145.
29 L. Chao, T. Niu, W. Gao, C. Ran, L. Song, Y. Chen and W. Huang, *Adv. Mater.*, 2021, **33**, 2005410.
30 J. Yang, E. L. Lim, L. Tan and Z. Wei, *Adv. Energy Mater.*, 2022, **12**, 2200975.
31 C. Liu, Y.-B. Cheng and Z. Ge, *Chem. Soc. Rev.*, 2020, **49**, 1653–1687.
32 S. Qiu, M. Majewski, L. Dong, D. Jang, V. M. L. Corre, J. G. Cerrillo, O. J. Ronsin, F. Yang, F. Guo, K. Zhang, L. Lüer, J. Harting, T. Du, C. J. Brabec and H.-J. Egelhaaf, *Adv. Energy Mater.*, 2024, **14**, 2303210.
33 Z. Yang, W. Zhang, S. Wu, H. Zhu, Z. Liu, Z. Liu, Z. Jiang, R. Chen, J. Zhou, Q. Lu, Z. Xiao, L. Shi, H. Chen, L. K. Ono, S. Zhang, Y. Zhang, Y. Qi, L. Han and W. Chen, *Sci. Adv.*, 2021, **7**, 3749.
34 Y. Xu, C. Zhou, X. Li, K. Du, Y. Li, X. Dong, N. Yuan, L. Li and J. Ding, *Small Methods*, 2024, **8**, 2400428.
35 Y. Jo, K. S. Oh, M. Kim, K. H. Kim, H. Lee, C. W. Lee and D. S. Kim, *Adv. Mater. Interfaces*, 2016, **3**, 1500768.
36 E. Q. Han, M. Lyu, E. Choi, Y. Zhao, Y. Zhang, J. Lee, S. M. Lee, Y. Jiao, S. H. A. Ahmad, J. Seidel, J. S. Yun, J. H. Yun and L. Wang, *Small*, 2023, **20**, 2305192.
37 N. K. Bansal, S. Porwal and T. Singh, *Surf. Interfaces*, 2024, **44**, 103738.
38 T. Wu, J. Wu, Y. Tu, X. He, Z. Lan, M. Huang and J. Lin, *J. Power Sources*, 2017, **365**, 1–6.
39 Z. Jiang, F. Ren, Q. Zhou, B. Wang, Z. Sun, M. Li, Z. Zhao, Z. Liu and W. Chen, *Adv. Energy Mater.*, 2025, **15**, 2500598.
40 S. J. Park, J. L. Eng, S. D. Pethe, D. J. J. Tay, N. Yantara and N. Mathews, *ChemSusChem*, 2025, **18**, 202402499.
41 S. Qiu, M. Majewski, L. Dong, A. Distler, C. Li, K. Forberich, J. Tian, N. H. Hemasiri, C. Liu, J. Zhang, F. Yang, V. M. L. Corre, M. Bibrack, R. Basu, A. Barabash, J. Harting, O. J. Ronsin, T. Du, H.-J. Egelhaaf and C. J. Brabec, *Energy Environ. Sci.*, 2025, **18**, 5926–5939.
42 H. Hu, D. B. Ritzer, A. Diercks, Y. Li, R. Singh, P. Fassl, Q. Jin, F. Schackmar, U. W. Paetzold and B. A. Nejand, *Joule*, 2023, **7**, 1574–1592.
43 F. Cataldo, *Eur. Chem. Bull.*, 2015, **4**, 92–97.
44 T. Bu, L. K. Ono, J. Li, J. Su, G. Tong, W. Zhang, Y. Liu, J. Zhang, J. Chang, S. Kazaoui, F. Huang, Y.-B. Cheng and Y. Qi, *Nat. Energy*, 2022, **7**, 528–536.
45 J. Chung, S. W. Kim, Y. Li, T. Mariam, X. Wang, M. Rajakaruna, M. M. Saeed, A. Abudulimu, S. S. Shin, K. N. Guye, Z. Huang, R. J. E. Westbrook, E. Miller, B. Subedi, N. J. Podraza, M. J. Heben, R. J. Ellingson, D. S. Ginger, Z. Song and Y. Yan, *Adv. Energy Mater.*, 2023, **13**, 2300595.
46 Y. Xiu, Y. Liu, K. Niu, J. Cui, Y. Qi, C. Lin, D. Chen, Y. Li, H. He, Z. Ye and Y. Jin, *ACS Mater. Lett.*, 2021, **3**, 1172–1180.
47 Y. Deng, C. H. Van Brackle, X. Dai, J. Zhao, B. Chen and J. Huang, *Sci. Adv.*, 2019, **5**, 7537.
48 Z. Liu, L. Qiu, L. K. Ono, S. He, Z. Hu, M. Jiang, G. Tong, Z. Wu, Y. Jiang, D.-Y. Son, Y. Dang, S. Kazaoui and Y. Qi, *Nat. Energy*, 2020, **5**, 596–604.
49 Y. Miao, M. Ren, Y. Chen, H. Wang, H. Chen, X. Liu, T. Wang and Y. Zhao, *Nat. Sustainability*, 2023, **6**, 1465–1473.

